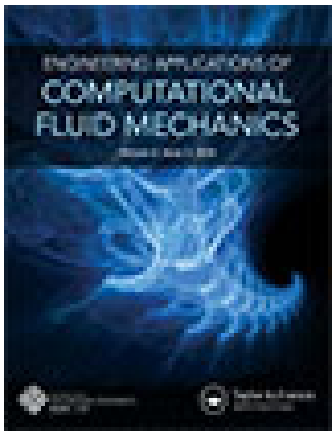

Engineering Applications of Computational Fluid Mechanics

Publication details, including instructions for authors and subscription information:
http://www.tandfonline.com/loi/tcfm20

SPH Modeling of Solid Boundaries Through a Semi-Analytic Approach

Antonio Di Monaco[a], Sauro Manenti[a], Mario Gallati[a], Stefano Sibilla[a], Giordano Agate[b] & Roberto Guandalini[b]

[a] Dipartimento di Ingegneria Idraulica e Ambientale, Università degli studi di Pavia, Via Ferrata, 1-27100 Pavia (Pv), Italy

[b] Environment and Sustainable Development Dept., ERSE s.p.a., Via Rubattino, 54-20134 Milan, Italy

Published online: 19 Nov 2014.

To cite this article: Antonio Di Monaco, Sauro Manenti, Mario Gallati, Stefano Sibilla, Giordano Agate & Roberto Guandalini (2011) SPH Modeling of Solid Boundaries Through a Semi-Analytic Approach, Engineering Applications of Computational Fluid Mechanics, 5:1, 1-15, DOI: 10.1080/19942060.2011.11015348

To link to this article: http://dx.doi.org/10.1080/19942060.2011.11015348

Engineering Applications of Computational Fluid Mechanics Vol. 5, No. 1, pp. 1–15 (2011)

SPH MODELING OF SOLID BOUNDARIES THROUGH A SEMI-ANALYTIC APPROACH

Antonio Di Monaco*, Sauro Manenti*+, Mario Gallati*, Stefano Sibilla*,
Giordano Agate** and Roberto Guandalini**

** Dipartimento di Ingegneria Idraulica e Ambientale, Università degli studi di Pavia, Via Ferrata, 1-27100 Pavia (Pv), Italy*
+ E-Mail: sauro.manenti@unipv.it (Corresponding Author)
*** Environment and Sustainable Development Dept., ERSE s.p.a., Via Rubattino, 54-20134 Milan, Italy*

ABSTRACT: This paper presents a general semi-analytic approach for modeling solid boundaries in the SPH method: boundaries are here considered as a material continuum with a suitable distribution of velocity and pressure; their contributions to each term of the SPH mass and momentum equations can be expressed in terms of a suitable integral extended to the part of the sphere of influence of the particle delimited by the boundary surface. Analytical details with reference to a slightly compressible viscous Newtonian fluid in three dimensions are given. The validity of the method is checked by comparing the obtained numerical results with available experimental data in a benchmark flow case.

Keywords: Newtonian fluid, solid boundary, smoothed particle hydrodynamics, 3D numerical modeling, model validation

1. INTRODUCTION

In the early applications of the Smoothed Particle Hydrodynamics (SPH) method to astrophysical problems (Lucy, 1977; Gingold and Monaghan, 1977) no solid boundaries had to be considered and, consequently, no methods for handling boundary conditions were needed. When the method was extended to confined fluid dynamics (Monaghan, 1992a), and in particular to free-surface hydrodynamics (Monaghan, 1992b), several approaches for treating boundary conditions were introduced. They can be essentially classified into the following four groups:

a. Ghost (or image) particles: this method appears to be the most rigorous as it yields a correct extension of pressure and velocity beyond the boundary. It is based on the generation, at each time step, of additional particles, as reflected images of the fluid particles located within a layer near the boundaries (seen as mirrors); the density (pressure) and velocity of each of these ghost particles are assigned so as to accomplish conditions of reflection or linear extension (Libersky et al., 1993; Randles and Libersky, 1996; Vila, 1999; Gallati and Braschi, 2002). Although this method can be easily implemented in two-dimensional (2D) geometries, in presence of straight boundary sides at right angles, and in three-dimensional (3D) geometries with plane boundary faces at right angles, its extension to the general case of 2D or 3D geometries with curved boundaries without right-angled edges appears to be indeed rather cumbersome and even problematic.

b. Boundary particles: this method consists in replacing solid boundaries by a system of external particles which can be either fixed or in motion (Monaghan, 1992b; Monaghan et al., 1999; Monaghan and Kos, 1999; Monaghan and Kos, 2000). The boundary particles, which have to fill a sufficiently thick layer, interact with the fluid particles through forces which depend on their relative distance; velocity and pressure of the boundary particles have to be properly assigned. The method is able to impose correct boundary conditions but requires an extra computational effort, in terms of storage and time, for handling the additional boundary particles; this drawback can become particularly severe in 3D.

c. Boundary forces: this method is based on the distribution of fixed "guard" particles along the boundaries, exerting suitable forces on the inner fluid particles (Monaghan, 1992b; Mosqueira et al., 2002; Monaghan et al.,

Received: 28 May 2010; Revised: 26 Jul. 2010; Accepted: 29 Jul. 2010

2003). These forces are empirically assigned depending on the nature of the problem as function of the distance between the boundary and the inner particles. Successful applications of this method to flows around arbitrarily convex and concave surfaces have been recently shown (Monaghan and Kajtar, 2009).

d. Boundary integrals: this method is based on a direct evaluation of the boundary contributions to the SPH approximation of the fluid-dynamic equations, without introducing any additional particle. There are few examples of such techniques in the literature, either limited to particular problems (Vila, 1999) or used to derive boundary contact forces (Kulasegaram et al., 2004). None of these approaches takes directly into account the boundary effect on the balance equations, apart from De Leffe et al. (2009), who evaluate the boundary contribution as a surface boundary integral and compute it through an SPH approximation, by discretizing the boundary with surface elements whose size is the same as the one of the particles.

In this paper we propose a general semi-analytical technique which overcomes the above limitations and drawbacks, in particular those arising in 3D problems with very irregular boundaries.

The philosophy of the method can be summarized as follows. The portions of the solid boundary which contribute to the mass and momentum equations of the generic particle can be replaced, just as in the ghost particle technique, by a fluid region which extends beyond the solid boundary: this virtual fluid region is treated as a material continuum (i.e. composed of an infinite number of particles) with a suitable distribution of velocity, density and pressure. The boundary contributions in the balance equations of each particle result therefore in integral terms extended to the portion of the sphere of influence of the particle lying beyond the boundary surface. These integral terms can be computed analytically and their value depends only on the geometry of the problem.

In this work analytical details are provided with reference to slightly compressible viscous Newtonian fluids in three dimensions, bearing in mind that concepts and formulas can be easily reduced to two dimensions; for sake of simplicity, the boundaries are thought of as composed of plane faces (triangles and quadrangles) even if the results hold also for curved boundary faces.

A comparison between numerical and experimental data for the dam-break wave problem developed by Kleefsman et al. (2005) is presented in order to prove the validity of the proposed method.

The paper has the following structure: section 2 presents the basic features of the SPH method and the geometrical scheme used to describe the relevant features of the semi-analytic approach. The boundary terms for the mass conservation equation are derived in section 3, while those for the momentum equation are derived in section 4. Section 5 shows the procedure for the numerical solution of the integrals recurring in the boundary terms of the conservation equations. Some additional features of the scheme concerning smoothing procedures and supplementary boundary forces are briefly recalled in section 6. In section 7 the numerical results are discussed and a comparison is made with the available experimental data for the selected benchmark dam-break test.

2. SPH BASICS AND GEOMETRICAL SCHEME

The SPH method analyzes the fluid flow by subdividing the continuum into "elementary" fluid particles of constant mass m which is not considered as concentrated in a single point in space, but is distributed (smoothed) around the center of mass of the particle itself, according to a smoothing (or kernel) function W defined on a compact support (Monaghan, 1992a). This support usually consists in a sphere (a circle in 2D) of radius R centered on the center of mass of the particle. Each particle interacts only with particles whose center of mass falls within its sphere of influence.

The value of the generic flow variable f at a point $\mathbf{x}$ can be therefore estimated by interpolation from the continuous values assumed within the sphere Ω of radius R=2h (where h is defined as the SPH *smoothing length*):

$$\langle f(\mathbf{x})\rangle = \int_{\Omega} f(\boldsymbol{\xi})\, W\left(|\mathbf{x}-\boldsymbol{\xi}|, h\right)\, d\boldsymbol{\xi} \tag{1}$$

or, in form of the discrete values pertaining to the N particles laying inside Ω:

$$\langle f\rangle = -\sum_{j=1}^{N} \frac{m_j}{\rho_j} f_j\, W\left(|\mathbf{x}-\mathbf{x}_j|, h\right) \tag{2}$$

where ρ is the density of the fluid. The derivatives of f can be approximated by SPH interpolation likewise (Liu and Liu, 2003).

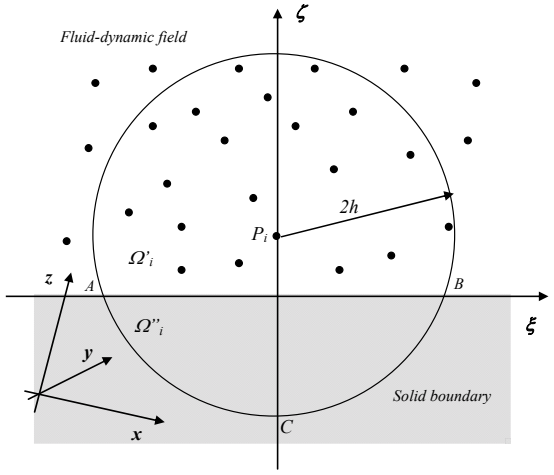

Fig. 1 Scheme of a generic particle P_i and neighboring particles in the vicinity of a plane solid boundary.

Fig. 1 shows schematically a generic particle P_i located near a plane boundary face, i.e. such that the relative distance d_i is less than the radius of influence of the particle R.

Let Ω_i be the sphere of influence of the particle P_i which has been split into two parts Ω'_i and Ω''_i, respectively inside and outside the flow-field; the surface AB is the portion of the boundary face within the sphere Ω_i.

Beside the global Cartesian frame of reference (x, y, z), whose unit vectors are (**i**, **j**, **k**), two local frames of reference can be defined; the first is the Cartesian frame (ξ, η, ζ) which has origin in the projection O' of P_i on the boundary surface and axis ζ normal to the boundary; the second is the spherical frame (r, ϑ, φ) centered on P_i. In the following the local Cartesian coordinates of the particle P_i will be indicated by (ξ_i, η_i, ζ_i), keeping in mind that $\xi_i = \eta_i = 0$ and $\zeta_i = d_i$, while the unit vectors of the local axes, with respect to the global frame of reference, are respectively **l**=(l_x, l_y, l_z), **m**=(m_x, m_y, m_z) and **n**=(n_x, n_y, n_z).

Of course, the following relations hold:

$$r = \sqrt{\left(\xi - \xi_i\right)^2 + \left(\eta - \eta_i\right)^2 + \left(\zeta - \zeta_i\right)^2}$$
$$\vec{\nabla} r = \begin{bmatrix} R_\xi & R_\eta & R_\zeta \end{bmatrix}^T = \mathbf{R} \qquad (3)$$

where the apex ^{T} denotes matrix transposition while **R** denotes the unit vector in the radial direction; $r_b(\vartheta, \varphi)$ indicates the distance from P_i to a generic point belonging to the boundary face.

In the following sections a uniform and constant mass force field is assumed (i.e. gravity) and the global Cartesian frame of reference is fixed with the z-axis directed upward. The application of the proposed boundary condition scheme to the case of a generic mass force field is straightforward.

3. BOUNDARY CONTRIBUTION TO THE MASS CONSERVATION EQUATION

The SPH discrete form of the mass conservation equation can be obtained through a discretization procedure which originates from a continuum form of the mass conservation law (Monaghan, 1992a). For the generic fluid particle P_i the mass conservation equation can be written in Lagrangian form by adopting a kernel approximation in Ω_i:

$$\frac{d\rho_i}{dt} = -\left\langle \rho \nabla \bullet \mathbf{v} \right\rangle_i = -\int_{\Omega_i} \rho(\mathbf{x}) \left[\mathbf{v}(\mathbf{x}) - \mathbf{v}_i \right] \bullet \vec{\nabla}_i W\left(|\mathbf{x} - \mathbf{x}_i|, h\right) d\Omega \qquad (4)$$

where **v** is velocity and **x** denotes the position of a generic integration point P inside Ω_i.

When the particle P_i is located near the boundary (Fig. 1) the integral in Eq. (4) can be split into two parts: the first, which is extended to the sub-domain Ω'_i, i.e. inside the flow-field, can be discretized by the usual SPH scheme; the second, which pertains to the sub-domain Ω''_i, i.e. the virtual fluid region extended outside the boundary, has to be treated separately. With this decomposition, Eq. (4) becomes:

$$\frac{d\rho_i}{dt} = -\sum_{j=1}^{N_i} m_j \left(\mathbf{v}_j - \mathbf{v}_i \right) \bullet \vec{\nabla}_i W\left(r_j, h \right) - \int_{\Omega''_i} \rho(\mathbf{x}) \left[\mathbf{v}(\mathbf{x}) - \mathbf{v}_i \right] \bullet \vec{\nabla}_i W\left(|\mathbf{x} - \mathbf{x}_i|, h\right) d\Omega \qquad (5)$$

where N_i denotes the number of the neighboring fluid particles P_j of P_i. The symbol $\vec{\nabla}_i$ denotes a gradient referred to the position of the particle P_i.

The boundary contribution in Eq. (5) can be evaluated by making some assumptions on the distribution of density and velocity in the virtual fluid region beyond the boundary; the simplest one reproduces, in a simplified way, the one adopted in the ghost particle method, i.e. $\rho(\mathbf{x}) \cong \rho_i$ and $\mathbf{v}(\mathbf{x}) \cong 2\mathbf{v}_b - \mathbf{v}_i$, where $\mathbf{v}_b$ is the velocity of the generic boundary face: ρ and **v** are therefore assumed to be uniformly distributed in Ω''_i.

If the local spherical frame of reference (r, ϑ, φ) is adopted, the integral on the right-hand side of Eq. (5) can be expressed as:

$$2\rho_i \left(\mathbf{v}_i - \mathbf{v}_b \right) \bullet \int_{\bar{\alpha}} \int_{r_b(\vartheta,\phi)}^{2h} \vec{\nabla} W\left(|\mathbf{x} - \mathbf{x}_i|, h\right) r^2 dr\, d\bar{\alpha} \qquad (6)$$

where the integration is extended to the solid angle $\overline{\alpha}(\vartheta,\varphi)$ under which the particle P_i "sees" the portion of the boundary face intercepted by the sphere of influence Ω_i.

By considering that $\vec{\nabla}W = \frac{dW}{dr}\vec{\nabla}r = \frac{dW}{dr}\mathbf{R}$, Eq. (6) can be written also as:

$$2\rho_i(\mathbf{v}_i - \mathbf{v}_b)\bullet\int_{\overline{\alpha}}\mathbf{R}(\vartheta,\phi)J_2(\vartheta,\phi)\,d\overline{\alpha} \tag{7}$$

where $J_2(\vartheta,\varphi) = \int_{r_b(\vartheta,\varphi)}^{2h}\frac{dW}{dr}r^2dr$. The analytical details for the calculation of the integral J_2 are provided in Section 5.

In the more general case of a particle P_i located near M boundary faces the boundary contribution will be expressed by a summation of M integrals, each extended to the solid angle $\overline{\alpha}_m$ relevant to the single face m; Eq. (4), with the boundary integral defined by Eq. (7), is generalized by:

$$\frac{d\rho_i}{dt} = -\sum_{j=1}^{N_i}m_j(\mathbf{v}_j - \mathbf{v}_i)\bullet\vec{\nabla}_i W(r_j,h) - 2\rho_i\sum_m\left(\mathbf{v}_i - \mathbf{v}_b^{(m)}\right)\bullet\int_{\overline{\alpha}_m}\mathbf{R}_m(\vartheta,\phi)J_2(\vartheta,\phi)\,d\overline{\alpha} \tag{8}$$

4. BOUNDARY CONTRIBUTION TO THE MOMENTUM EQUATION

The SPH form of the momentum equation for slightly compressible fluids can be obtained through a discretization procedure of the continuum form:

$$\frac{d\mathbf{v}_i}{dt} = -<\frac{1}{\rho}\nabla p>_i + <\nu\nabla^2\mathbf{v}>_i + <\nu'\nabla(\nabla\bullet\mathbf{v})>_i - g\mathbf{k} \tag{9}$$

where

$$\nu' = \frac{\nu}{3} + \alpha_M c_0 h \quad \text{for} \quad (\mathbf{v}_j - \mathbf{v}_i)\bullet(\mathbf{x}_j - \mathbf{x}_i) < 0$$
$$\nu' = \frac{\nu}{3} \quad \text{for} \quad (\mathbf{v}_j - \mathbf{v}_i)\bullet(\mathbf{x}_j - \mathbf{x}_i) \geq 0 \tag{10}$$

In Eq. (9), ν represents the kinematic viscosity of the fluid while the coefficient ν' includes the artificial viscosity term introduced by Monaghan (1992a) for stability reasons as defined in Eq. (10): α_M is a non-dimensional coefficient and c_0 is the speed of sound in the fluid, given by $c_0 = \sqrt{\varepsilon/\rho}$, where ε is the compressibility coefficient.

The pressure gradient force, the volume viscosity force and the shear viscosity force terms in Eq. (9) can be computed by adopting a decomposition for the contribution of the fluid inside and outside the boundary similar to the one discussed in the previous section:

$$-<\frac{1}{\rho}\nabla p>_i = -\sum_{j=1}^{N_i}m_j\left(\frac{p_i}{\rho_i^2} + \frac{p_j}{\rho_j^2}\right)\vec{\nabla}_i W(r_j,h) - \int_{\Omega''_i}\rho\left(\frac{p}{\rho^2} + \frac{p_i}{\rho_i^2}\right)\vec{\nabla}_i W(r,h)\,d\Omega \tag{11}$$

$$<\nu\nabla^2\mathbf{v}>_i = \nu\sum_{j=1}^{N_i}\frac{m_j}{\rho_i r_j^2}(\mathbf{v}_j - \mathbf{v}_i)\bullet(\mathbf{x}_j - \mathbf{x}_i)\vec{\nabla}_i W(r_j,h) + \nu\int_{\Omega''_i}\frac{1}{r^2}(\mathbf{v} - \mathbf{v}_i)\bullet(\mathbf{x} - \mathbf{x}_i)\vec{\nabla}_i W(r,h)\,d\Omega \tag{12}$$

$$<\nu'\nabla(\nabla\bullet\mathbf{v})>_i = -2\nu'\sum_{j=1}^{N_i}\frac{m_j}{\rho_i r_j}(\mathbf{v}_j - \mathbf{v}_i)\frac{\partial W}{\partial r} - 2\nu'\int_{\Omega''_i}(\mathbf{v} - \mathbf{v}_i)\frac{1}{r}\frac{\partial W}{\partial r}d\Omega \tag{13}$$

The shear viscosity term is here discretized according to the formulation of Morris et al. (1997).

In the following subsections, the boundary integrals in the Eqs. (11)-(13) will be derived according to the scheme shown in Section 3; the analytical details of the integration procedure are explained in Section 5.

4.1 Pressure gradient force term

The boundary contribution to the pressure gradient term Eq. (11) is here obtained by assuming that, inside the sub-domain Ω''_i, the density has a uniform distribution (i.e. $\rho=\rho_i$) while the pressure has a linear variation according to the hydrostatic gradient:

$$p = p_i - \rho g r\,\mathbf{R}\bullet\mathbf{k} \tag{14}$$

With the abovementioned assumptions the integral on the right-hand side of Eq. (11) can be transformed into:

$$\int_{\Omega''_i}\rho\left(\frac{p}{\rho^2} + \frac{p_i}{\rho_i^2}\right)\vec{\nabla}_i W(r,h)\,d\Omega = \frac{2p_i}{\rho_i}\int_{\Omega''_i}\vec{\nabla}_i W\,d\Omega - g\int_{\Omega''_i}\mathbf{R}\bullet\mathbf{k}\,r\vec{\nabla}_i W\,d\Omega \tag{15}$$

The integrals on the right-hand side of Eq. (15) can be solved in the local spherical frame of reference (r, ϑ, φ) as illustrated in the previous section, leading to:

$$\int_{\Omega''_i}\rho\left(\frac{p}{\rho^2}+\frac{p_i}{\rho_i^2}\right)\vec{\nabla}_i W(r,h)\,d\Omega = -\frac{2p_i}{\rho_i}\int_{\bar{\alpha}}\mathbf{R}\,J_2(\vartheta,\phi)\,d\bar{\alpha}+g\left[\int_{\bar{\alpha}}\mathbf{R}\mathbf{R}^T J_3(\vartheta,\phi)\,d\bar{\alpha}\right]\mathbf{k} \tag{16}$$

where the dependency of $\mathbf{R}$ on ϑ and φ will be omitted for simplicity, here and in the following, and $J_3(\vartheta,\varphi)=\int_{r_b(\vartheta,\varphi)}^{2h}\frac{dW}{dr}r^3dr$.

As already pointed out for the boundary contribution to the mass conservation equation, in the most general case of a particle P_i located close to M boundary faces, Eq. (16) must be replaced by a summation of M contributions, each related to the m^{th} face.

Thus the SPH approximation of the pressure gradient term for a particle P_i located near to M boundary faces becomes:

$$<\frac{1}{\rho}\vec{\nabla}p>_i=\sum_{j=1}^{N_i}m_j\left(\frac{p_i}{\rho_i^2}+\frac{p_j}{\rho_j^2}\right)\vec{\nabla}_i W\left(r_j,h\right) +\sum_m\left\{\begin{array}{l}-\frac{2p_i}{\rho_i}\int_{\bar{\alpha}_m}\mathbf{R}_m\,J_2\,d\bar{\alpha}\\ +g\left[\int_{\bar{\alpha}_m}\mathbf{R}_m\,\mathbf{R}_m^T J_3\,d\bar{\alpha}\right]\mathbf{k}\end{array}\right\} \tag{17}$$

4.2 Viscosity force terms

By repeating the same steps shown above in the local spherical frame of reference (r, ϑ, φ), the integral on the right-hand side of Eq. (12) becomes, in the general case for M neighboring boundary faces:

$$\nu\int_{\Omega''_i}\frac{1}{r^2}\left(\mathbf{v}-\mathbf{v}_i\right)\bullet\left(\mathbf{x}-\mathbf{x}_i\right)\vec{\nabla}_i W\left(r,h\right)d\Omega = +2\nu\sum_m\left(\int_{\bar{\alpha}_m}\mathbf{R}_m\,\mathbf{R}_m^T J_1\,d\bar{\alpha}\right)\left(\mathbf{v}_i-\mathbf{v}_b^{(m)}\right) \tag{18}$$

where $J_1(\vartheta,\varphi)=\int_{r_b(\vartheta,\varphi)}^{2h}\frac{dW}{dr}r\,dr$, while the integral term on the right-hand side of Eq. (10) yields:

$$-2\nu'\int_{\Omega''_i}\left(\mathbf{v}-\mathbf{v}_i\right)\frac{1}{r}\frac{\partial W}{\partial r}d\Omega = -2\nu'\sum_m\left(\int_{\bar{\alpha}_m}J_1\,d\bar{\alpha}\right)\left(\mathbf{v}_b^{(m)}-\mathbf{v}_i\right) \tag{19}$$

The virtual velocity field in the fluid domain extended outside the boundary can be extrapolated, in analogy with the ghost particle method, as follows:

$$\mathbf{v}-\mathbf{v}_i=\left[\begin{array}{c}\phi_S\left(2v_{b\xi}-v_{i\xi}\right)+\left(1-\phi_S\right)v_{i\xi}-v_{i\xi}\\ \phi_S\left(2v_{b\eta}-v_{i\eta}\right)+\left(1-\phi_S\right)v_{i\eta}-v_{i\eta}\\ \left(2v_{b\zeta}-v_{i\zeta}\right)-v_{i\zeta}\end{array}\right] =\left[\begin{array}{c}\phi_S\,2\left(v_{b\xi}-v_{i\xi}\right)\\ \phi_S\,2\left(v_{b\eta}-v_{i\eta}\right)\\ 2\left(v_{b\zeta}-v_{i\zeta}\right)\end{array}\right] \tag{20}$$

where ($v_{b\xi}$, $v_{b\eta}$, $v_{b\zeta}$) are the components of the boundary velocity in the local frame of reference. The "shear" coefficient φ_s allows us to simulate the "free slip" condition for φ_s=0 and the "no-slip" condition for φ_s=1; any other intermediate condition can be obtained for $0<\varphi_s<1$.

5. COMPUTATION OF THE INTEGRAL BOUNDARY TERMS

For the analytical calculation of the integrals in the boundary contribution terms of the mass and momentum balance equation it is convenient to refer vectors and operators to the local Cartesian frame of reference (ξ,η,ζ).

The results shown in the present paper were obtained by adopting the cubic spline kernel function proposed by Monaghan (1992a):

$$W(r,h)=\frac{k}{h^s}\left\{\begin{array}{ll}1-\frac{3}{2}\left(\frac{r}{h}\right)^2+\frac{3}{4}\left(\frac{r}{h}\right)^3 & \text{for}\quad 0\le r\le h\\ \frac{1}{4}\left(2-\frac{r}{h}\right)^3 & \text{for}\quad h\le r\le 2h\\ 0 & \text{for}\quad r\ge 2h\end{array}\right. \tag{21}$$

with $k=\frac{10}{7\pi}$ and s=2 in 2D and $k=\frac{1}{\pi}$ and s=3 in 3D. All the analytical formulas obtained in the following were derived for the kernel function Eq. (21); of course, analogous formulas may be

derived for any other kernel function commonly used.

A normalized kernel function can be defined by:

$$\frac{1}{h^s}\bar{W}(\tilde{r}) = W(r,h) \tag{22}$$

where $\tilde{r} = r/h$; it follows that:

$$\frac{dW}{dr} = \frac{1}{h^s}\frac{d\bar{W}}{d\tilde{r}}\frac{d\tilde{r}}{dr} = \frac{1}{h^{s+1}}\frac{d\bar{W}}{d\tilde{r}} \tag{23}$$

As already said, the integration of the boundary terms in the mass and momentum balance equations is best obtained by adopting the local spherical frame of reference (r,ϑ,φ) centered on particle P_i, where $0 \le \vartheta < 2\pi$ is the longitude and $-\pi/2 \le \varphi \le \pi/2$ is the latitude, as shown in Fig. 2.

The elementary volume can be generally expressed by $d\Omega = r^2 dr d\bar{\alpha}$, where $d\bar{\alpha} = \cos\varphi\, d\varphi\, d\vartheta$ is the elementary solid angle linked to the spatial direction of the oriented segment $\overrightarrow{P_iP}$, defined by (ϑ,φ).

The analytical solution of the integrals at the right-hand side of Eqs. (7), (16), (18) and (19) can be reduced to the calculation of the generic expression in Eq. (24) which is obtained by introducing the above mentioned local spherical frame of reference centered on particle P_i and by considering the well-known property $\vec{\nabla}_i W = -\vec{\nabla} W$ of the kernel function:

$$\int_{\bar{\alpha}} \mathbf{A}\left(\int_{r_b}^{2h} \frac{dW}{dr} r^n\, dr\right) d\bar{\alpha} \tag{24}$$

The outer integral in Eq. (24) is extended to the solid angle $\bar{\alpha}$ under which the particle P_i "sees" the portion of the boundary face intercepted by the sphere of influence Ω_i and $\mathbf{A}$ denotes a generic tensor of order zero to two depending on the circumstances; the inner integral ranges from r_b, distance between the particle P_i and the intersection of the generic radius issuing from P_i with the boundary face, to the radius of the kernel support $2h$ and can be easily expressed analytically in terms of the normalized kernel Eq. (22):

$$\int_{r_b}^{2h} \frac{dW}{dr}\, r^n\, dr = \frac{1}{h^{s-n}} \int_{\tilde{r}_b}^{2} \frac{d\bar{W}}{d\tilde{r}}\, \tilde{r}^n\, d\tilde{r} \equiv J_n(\tilde{r}_b) \tag{25}$$

When the cubic-spline kernel function Eq. (21) is adopted, the analytical solution of the integral at the right-hand side of Eq. (25) yields:

for n=1

$$J_1(\tilde{r}_b) = \frac{1}{\pi}\begin{cases} -\frac{3}{4} + \tilde{r}_b^3 - \frac{9}{16}\tilde{r}_b^4 & 0 \le \tilde{r}_b < 1 \\ -1 + \frac{3}{2}\tilde{r}_b^2 - \tilde{r}_b^3 + \frac{3}{16}\tilde{r}_b^4 & 1 \le \tilde{r}_b < 2 \\ 0 & 2 \le \tilde{r}_b \end{cases} \tag{26}$$

for n=2

$$J_2(\tilde{r}_b) = \frac{1}{\pi}\begin{cases} -\frac{7}{10} + \frac{3}{4}\tilde{r}_b^4 - \frac{9}{20}\tilde{r}_b^5 & 0 \le \tilde{r}_b < 1 \\ -\frac{4}{5} + \tilde{r}_b^3 - \frac{3}{4}\tilde{r}_b^4 + \frac{3}{20}\tilde{r}_b^5 & 1 \le \tilde{r}_b < 2 \\ 0 & 2 \le \tilde{r}_b \end{cases} \tag{27}$$

and for n=3

$$J_3(\tilde{r}_b) = \frac{1}{\pi}\begin{cases} -\frac{3}{4} + \frac{3}{5}\tilde{r}_b^5 - \frac{3}{8}\tilde{r}_b^6 & 0 \le \tilde{r}_b < 1 \\ -\frac{4}{5} + \frac{3}{4}\tilde{r}_b^4 - \frac{3}{5}\tilde{r}_b^5 + \frac{1}{8}\tilde{r}_b^6 & 1 \le \tilde{r}_b < 2 \\ 0 & 2 \le \tilde{r}_b \end{cases} \tag{28}$$

The outer integral extended to the solid angle $\bar{\alpha}$ must be solved numerically. A simple algorithm consists in dividing the surface of the sphere of

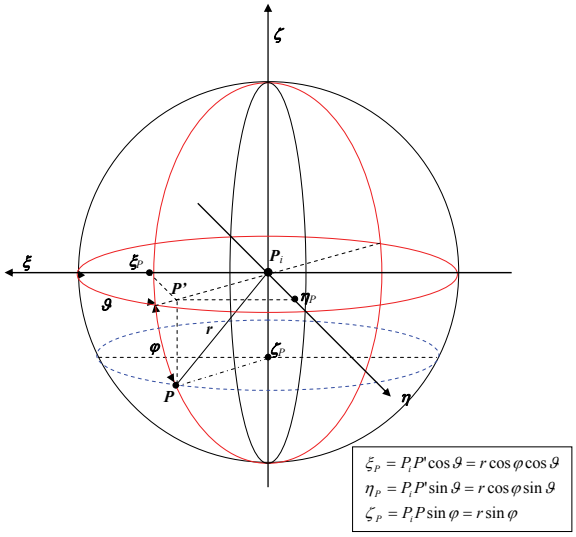

Fig. 2 Orthogonal and spherical reference frames linked to particle P_i.

influence Ω_i in a sufficient number of facets, and approximating the integrals by summations extended to these facets. This subdivision can be obtained by means of a mesh of uniformly spaced meridians ad parallels; it is sufficient to confine this mesh to the half-sphere defined as a set of points $P \equiv (r_P, \vartheta_P, \varphi_P)$ such that: $r_P = |P_i P| = 2h = R$, $0 \le \vartheta_P < 2\pi$ and $-\pi/2 \le \varphi_P \le 0$. Therefore, if n_ϑ indicates the number of spherical wedges and n_φ the number of spherical zones, the constant longitude and latitude intervals are respectively $\Delta\vartheta = 2\pi / n_\vartheta$ and $\Delta\varphi = \pi / 2n_\varphi$. The essential data of the k^{th} facet are:

a. The local Cartesian coordinates of the facet centre $P_k(\varphi_k, \vartheta_k)$, given by:

$$\begin{aligned} \xi_k &= R\cos\phi_k \cos\vartheta_k \\ \eta_k &= R\cos\phi_k \sin\vartheta_k \\ \zeta_k &= R\sin\phi_k \end{aligned} \tag{29}$$

b. The related solid angle, given by:

$$\Delta\bar{\alpha}_k = 2\cos\phi_k \sin\frac{\Delta\phi}{2}\Delta\vartheta \tag{30}$$

c. The three components of the unit vector $\mathbf{R}_k$ of the segment P_iP_k given by:

$$\begin{aligned} R_{\xi k} &= \xi_k / R = \xi_k / 2h \\ R_{\eta k} &= \eta_k / R = \eta_k / 2h \\ R_{\zeta k} &= \zeta_k / R = \zeta_k / 2h \end{aligned} \tag{31}$$

In this way, all of the data needed to perform the summations are available. To identify the portion of the boundary face *m* which gives a contribution to the particle P_i, we have to find, for each facet *k*, the point of intersection Q_k of the segment P_iP_k with the boundary face *m* and include this facet in the summations only if the point Q_k belongs both to the sphere Ω_i (i.e. $r_b < R$) and to the face *m*.

After several numerical experiments on 3D geometries, it was found that it is sufficient to assign $n_\vartheta = 16$ and $n_\varphi = 4$, i.e. 64 integration points (facets), to achieve a satisfactory approximation of the boundary integrals.

6. ADDITIONAL FEATURES

The computational stability of the numerical SPH algorithm is commonly improved by including a step for density or velocity smoothing (or both) (Gingold and Monaghan, 1977; Randles and Libersky, 1996). The application of the smoothing scheme near the boundary needs, for consistency, the introduction of suitable terms which take into account its contribution. For the sake of brevity we do not provide here the relevant details, as these terms can be easily derived by applying the same concepts shown above.

At each time step, the generic flow variable *f* of a particle *i* can be smoothed by a linear combination of its value f_i and the value obtained by SPH interpolation on the N_i surrounding particles. The smoothed value is expressed by:

$$\hat{f}_i = (1-\theta_f)\, f_i + \theta_f \frac{\sum_{j=1}^{N} \frac{m_j}{\rho_j} f_j\, W(r_j, h)}{\sum_{j=1}^{N} \frac{m_j}{\rho_j} W(r_j, h)} \tag{32}$$

where θ_f is a smoothing parameter.

For a particle lying close to the boundary, Eq. (32) becomes:

$$\hat{f}_i = (1-\theta_f)\, f_i + \theta_f \frac{\sum_{j=1}^{N} \frac{m_j}{\rho_j} f_j\, W(r_j, h) + \int_{\Omega_i''} f\, W(r, h)\, d\Omega}{\sum_{j=1}^{N} \frac{m_j}{\rho_j} W(r_j, h) + \int_{\Omega_i''} W(r, h)\, d\Omega} \tag{33}$$

When a convenient boundary value f_b is assumed in the virtual flow region beyond the boundary, the integral terms in Eq. (33) can be reduced, with the usual notation, to the general form:

$$\int_{\alpha} \int_{r_b}^{2h} W\, r^n\, dr\, d\alpha \tag{34}$$

which can be integrated through the analytical-numerical procedure described in section 5.

Another question to be pointed out concerns the boundary ability to keep particles in the computational domain, i.e. to avoid particle escape. Such containment task should be carried out by the combined action of the boundary contributions to both mass conservation Eq. (3) and pressure gradient force Eq. (15). This generally occurs in the usual condition, i.e. when there is a sufficient number of particles around the particle P_i, such that the inner sub-domain Ω'_i is fully occupied by particles.

On the other hand, if there are only a few neighboring particles and both the normal velocity of the particle P_i is close to zero and the normal component of gravity is directed against

the wall, the particle P_i may cross the boundary wall. To avoid this shortcoming, it can be useful to add an elastic reaction normal to the boundary which depend on the distance ζ_i of the particle P_i from the boundary face; to minimize any possible resulting perturbation, this reaction should act only when the distance become less then a minimum value $\zeta_{\min}$ set as a suitable fraction of the smoothing length h.

We have devised, for R_{ci} (the "normal reaction"), the following expression:

$$R_{ci} = 0 \qquad for\ \zeta_i \geq \zeta_{min}$$

$$R_{ci} = -\frac{c_0^2}{h} ln \frac{h - \zeta_{min} + \zeta_i}{h} \cong \frac{c_0^2}{h} \frac{\zeta_{min} - \zeta_i}{h} \quad for\ \zeta_i < \zeta_{min} \tag{35}$$

which simulates the elastic reaction of a column of height h of fluid with the same compressibility as the fluid of particle P_i. Eq. (35) works well without introducing additional stability requirements to the time step.

7. VALIDATION OF THE METHOD

In order to show the validity of the described procedure, the SPH simulation of a reference benchmark test-case has been carried out: the obtained results are compared with available experimental data and discussed in this section after a brief description of the facility, including the model geometry and parameters.

Other applications of the present method for handling boundary conditions, which include comparisons with experimental data, are shown in Manenti et al. (2009).

7.1 Description of the test-case

Among the several SPH benchmark test-cases defined by the SPHERIC ERCOFTAC Special Interest Group, the attention is focused here on the 3D dam-break problem proposed by Kleefsman et al. (2005).

The test-case has been set up in order to reproduce the laboratory experiment performed at the Maritime Research Institute Netherlands (MARIN): such a flow aims at reproducing the relevant aspects of green water flow on the deck of a ship.

Fig. 3 depicts the geometry of the facility described in Kleefsman et al. (2005) and has been adopted for the run as such. The tank is 3.22m long, 1.00m wide and 1.00m deep. Water particles are free to leave the basin from the open roof.

In the original experiment, placed near the right-hand side of the tank, confines water of depth 0.55m at rest. When the gate is suddenly opened by releasing a weight, a water tongue moves toward the left-hand side of the tank near which a fixed, rigid box has been placed to mimic a scale model of a container on the deck of a ship.

During the laboratory experiment water heights, pressures and forces have been measured as shown in Fig. 3 in which four vertical level probes (H1 to H4) have been used. The box was also covered by eight pressure sensors (P1 to P8), four on the front of the box and four on the top.

It must be pointed out that the SPH simulation here presented reproduces the geometrical features of the tank and of the obstacle along with the gauge positions, while the gate that initially confines the water column is not present such that the computation starts the fluid is free to collapse under the gravity force as in Lee et al. (2010).

Table 1 summarizes the values of both physical and numerical parameters adopted for the computation. Two non-dimensional parameters, which represent the pressure ϑ_p and the velocity ϑ_v smoothing coefficients adopted in the computation, are included; no friction is introduced at the bottom of the tank.

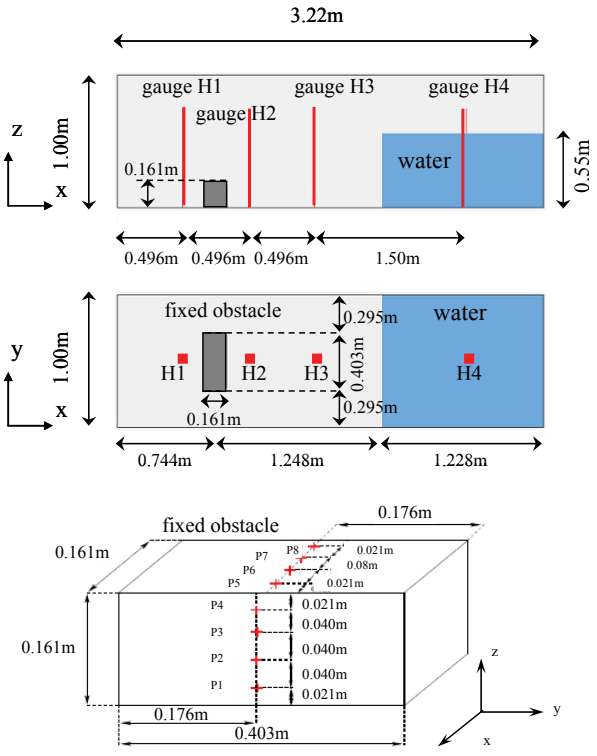

Fig. 3 Geometrical sketch of the test and gauges distribution.

Table 1 Summary of the model parameters: (a) 85400 fluid particles, (b) 676500 fluid particles.

δ [m]	h [m]	Δt [s]	ρ [kg/m^3]	α_M [−]	ε [Pa]	c_s [m/s]	μ [Pa s]	ϑ_v [−]	ϑ_p [−]
0.02 (a)	0.024 (a)	0.002715 (a)	1000.0	0.05	1.0E+5	60.0	1.0E-3	0. 3	0. 3
0.01 (b)	0.012 (b)	0.001018 (b)							

Fluid particles are placed at the nodes of a regular Cartesian grid with a mesh size of δ=0.02m (i.e. 1/8 of the length of the shorter box edge at the tank bottom, Fig. 3) resulting in a total number of 85400. An additional analysis has been carried out for investigating the effect of an increased particle resolution (676500) on the prediction of both water level and pressure at the probes as discussed in the following.

The smoothing length has been assumed equal to h=1.2δ. During the tuning of the model, this choice assured a proper number of neighbors regardless of the particle resolution.

The numerical scheme for time integration is a staggered first-order explicit scheme where the velocity of each particle is calculated at mid time-step with respect to both position and density:

$$\mathbf{v}_i^{(n+0.5)} = \mathbf{v}_i^{(n-0.5)} + \frac{t^{(n+1)} - t^{(n-1)}}{2}\left(\frac{d\mathbf{v}_i}{dt}\right)^{(n)}$$

$$\text{with} \quad \left(\frac{d\mathbf{v}_i}{dt}\right)^{(n)} = f(\mathbf{x}_i^{(n)}, \mathbf{v}_i^{(n-0.5)}, \rho_i^{(n)})$$

$$\mathbf{x}_i^{(n+1)} = \mathbf{x}_i^{(n)} + \left(t^{(n+1)} - t^{(n)}\right)\mathbf{v}_i^{(n+0.5)} \qquad (36)$$

$$\rho_i^{(n+1)} = \rho_i^{(n)} + \left(t^{(n+1)} - t^{(n)}\right)\left(\frac{d\rho_i}{dt}\right)^{(n+0.5)}$$

$$\text{with} \quad \left(\frac{d\rho_i}{dt}\right)^{(n+0.5)} = f(\mathbf{x}_i^{(n+1)}, \mathbf{v}_i^{(n+0.5)})$$

the superscripts denote here the time instants at which variables are evaluated.

From the updated density the pressure field is evaluated by means of the state equation for a weakly compressible fluid:

$$p_i = p_{0\,i} + \frac{\varepsilon}{\rho}\cdot\left(\rho_i - \rho_{0\,i}\right) \qquad (37)$$

in which ε is the compressibility modulus of the fluid and the subscript 0 denotes a reference value of pressure and density. Such a linear formulation can be adopted since percentage fluctuations around p_0 are small.

Since this scheme is conditionally stable, the Courant–Friedrichs–Lewy condition has to be satisfied together with the viscous stability condition:

$$\Delta t \le \min\left\{\frac{\delta}{c_s + |\mathbf{v}_{\max}|}, \frac{\rho h^2}{0.5\,\mu}\right\} \qquad (38)$$

in which $\mathbf{v}_{max}$ is the characteristic maximum velocity of the problem under investigation (assumed equal to the square root of the modulus of gravitational acceleration times the initial height of the collapsing water column), c_s is the sound speed and μ is the fluid dynamic viscosity.

The total CPU time is about 4 hours with 85400 fluid particles, and about 80 hours with 676500 fluid particles on a dualcore 3.6Ghz processor (4Gb RAM) for six seconds of simulation.

For more details on the pressure and velocity smoothing procedure the reader is referred to Manenti et al. (2009).

The free surface profile at every time step is determined by searching the position of the center of mass corresponding to the highest water particle falling within an horizontal distance of h with respect to the axis of each of the four probes (H1 to H4).

7.2 Comparison with experiments

Fig. 4 shows the comparison of the computed free surface and pressure field with the experimental results available from Kleefsman et al. (2005). It can be noted that, at t=0.4 s, the SPH model underestimates the velocity of the water front which appears to be slightly delayed with respect to the corresponding experimental frame.

Furthermore, after the impact with the fixed rigid box a significant air entrapment in the upward water jet can be noticed at t=0.6 s. Since such a phenomenon affects the loads on the obstacle after that time and due to the fact that in this model the air phase is neglected, those aspects may be responsible for some discrepancies between computed and measured pressure as discussed in the next section.

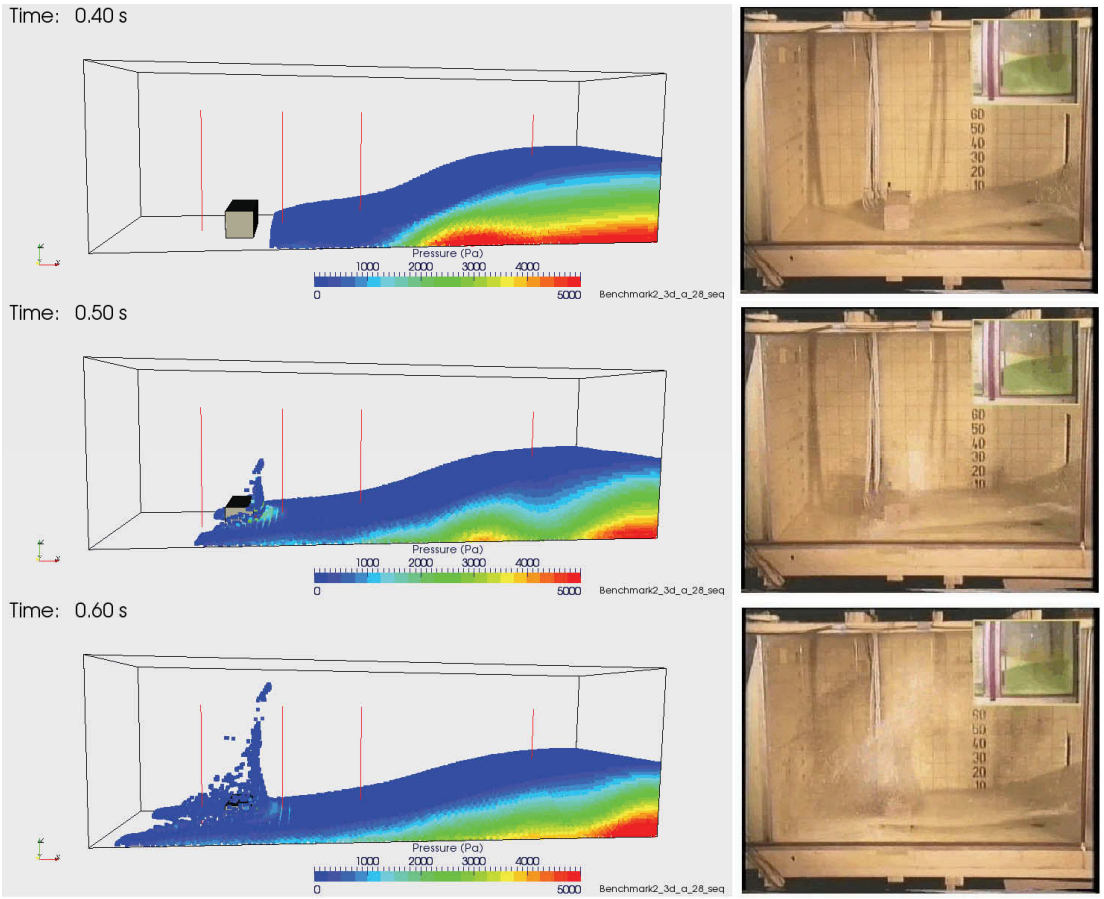

Fig. 4 Comparison of computed surface profile and pressure (85400 fluid particles) with experimental frames at t=0.4 s, t=0.48 s and t=0.60 s (Kleefsman et al., 2005).

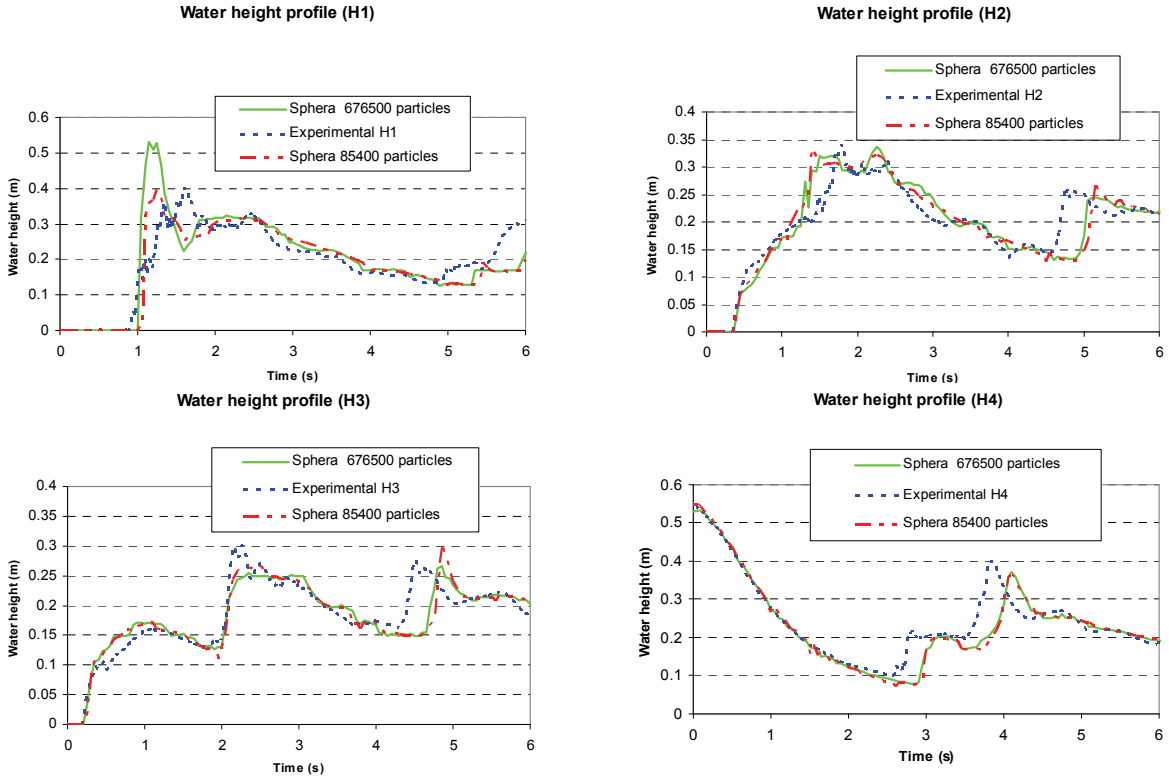

Fig. 5 Comparison between measured water height profiles at the gauges and calculated with different particle resolution.

Fig. 5 shows the comparison between calculated and measured water height at the four gauges in the tank (Fig. 3).

At gauge H1 the model output reproduces with a good accuracy the starting phase of the phenomenon between the incoming of the water wedge and the initial rising of the level; even the highest peak is matched at 0.4m but is expected in advance of about 0.4s with respect to the laboratory data. The second peak occurring at $t \approx 2.5$ s is very close to the one of the experimental curve which, however, shows a quicker rise. In the decreasing phase the numerical curve is close to the experiment but the latter ends before $t=5$ s. After that time it grows to a final maximum which is about 1.5 times the numerical one.

At gauge H2 the comparison allows us to make similar comments for what concerns the initial description of the phenomenon. The arrival of water is correctly predicted along with the maximum height of about 0.35m which, however, still anticipates the measured one. The curves show a similar trend in the decreasing phase even if its duration appears to be longer in the numerical simulation: actually, the last peak occurs after $t=5$ s. This phenomenon has been pointed out also by Lee et al. (2010). They have performed the same benchmark test simulation adopting a weakly compressible SPH model with a first-order explicit scheme for solving the balance equations in time but using a different treatment of the solid boundaries based on the adoption of ghost particles. In their model the smoothing length is $h=0.0275$ m, the initial particle spacing is about $\delta=0.018333$ m, the total number of the fluid particles is 108540 (plus 38142 wall particles and 113592 fictitious particles) and the time integration step is $\Delta t=1.8333\text{e-}4$ s.

At gauge H3 the two curves are rather close to each other until $t=4$ s, except that the second peak is underestimated. After that time, the numerical result seems to be shifted backward in time as noticed in the previous case: also at this gauge, the last peak occurs close to $t=5$ s and is fairly overestimated.

The calculated water level at the gauge H4, which is initially submerged, fits the experimental curve with a good accuracy up to about $t=2.5$ s. After that time, the curves seem to be shifted, the experimental one being in advance, and an underestimation of the last peak is noticed, similar to the results shown by Lee et al. (2010) with their weakly compressible model.

As noted by Kleefsman et al. (2005), the use of a coarse grid in their VOF simulation resulted in an underprediction of water speed; accordingly, an improvement in the prediction of the free surface profiles at the four gauges could be obtained by increasing the number of water particles.

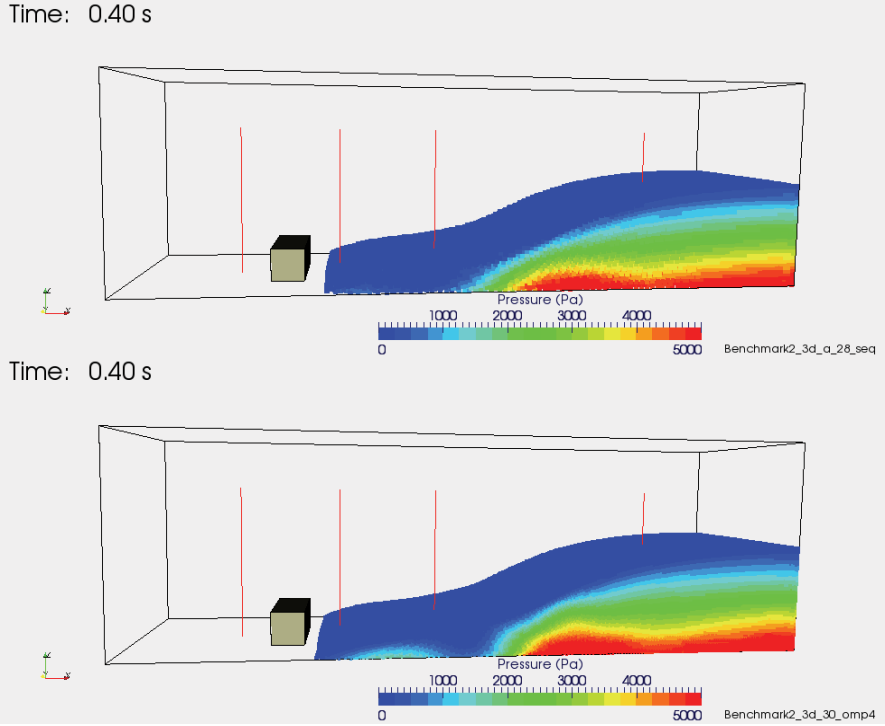

Fig. 6 Simulated pressure field and free surface profile at time $t=0.4$ s after the water release (upper panel, 85400 fluid particles; lower panel, 676500 fluid particles).

Actually, the lower panel in Fig. 6 displays the free surface profile at t=0.40 s obtained by increasing the number of fluid particles to 676500 in order to prove the mentioned hypothesis. The comparison with the upper panel (reproducing the one in Fig. 4 at t=0.40 s) shows that the speed of the water tongue increases with particle resolution. The continuous green line in Fig. 5 shows that except for a significant increase of the absolute maximum occurring before t=2.0 s, the behavior of predicted water level at H1 is somewhat similar to the previous analysis. The relative peak around t=5.0 s is slightly anticipated but is still late with respect to the experimental curve. A similar observation is valid for gauges H2 and H3 where the relative peak is fairly underestimated. No significant difference is appreciable for gauge H4.

Fig. 7 shows the comparison between calculated and measured pressure at the four gauges located on the bottom obstacle.

At gauge P1 the comparison shows that in both analyses a slight overestimation of the highest pressure peak occurs immediately after the water impact (t=0.5 s); subsequently the simulation with 676500 water particles is much closer to the experimental curve until t=1.0 s. After that the two numerical solutions become quite similar but the last peak occurring after t=5.0 s is better predicted with the higher resolution.

At gauge P3 the simulation with 676500 water particles leads to an underestimation of the maximum before t=1.0 s. After that time a similar observation to that of gauge P1 can be made, including the prediction of the last peak around t=5.0 s.

Regarding gauge P5, the pressure fluctuations before the first peak are drastically reduced in the 676500 water particles simulation; subsequently the numerical results are very close to each other and after t=5.0 s, the curve obtained with a higher resolution is much closer to the experimental one.

Finally at gauge P7 the curve obtained with 85400 water particles shows reduced pressure fluctuations before the first peak but a fictitious maximum still appears at about t=1.5 s. After that time both analyses provide a good prediction of the experimental pressure until t=5.0 s, but the last peak is slightly shifted backward, especially in the analysis with the coarser resolution.

It should be noted that the significant and unphysical pressure fluctuations obtained before t=1.5 s at gauges P5 and P7 are reported also in the work of Lee et al. (2010) when using either a weakly compressible or a truly incompressible SPH model.

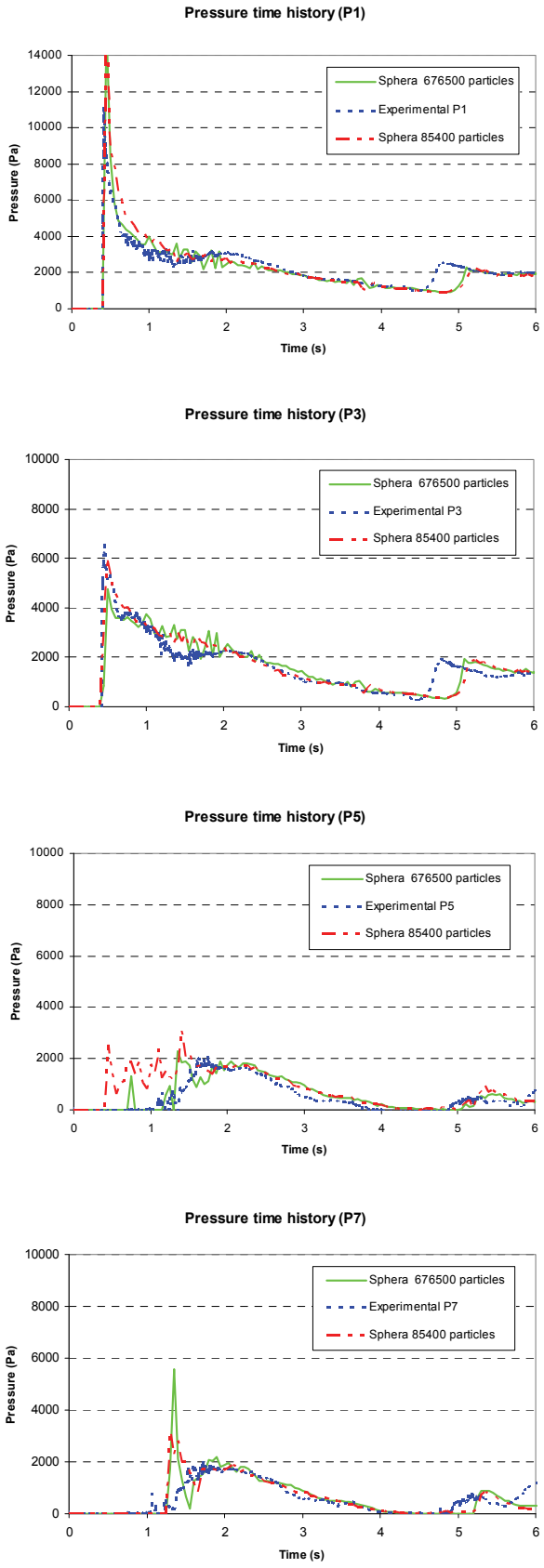

Fig. 7 Comparison between measured pressure profiles at the gauges and calculated with different particle resolution.

A comparison with those results shows that the approach proposed here for the weakly incompressible SPH method has the advantage of eliminating such oscillations at gauges P1 and P3 and reducing them at gauges P5 and P7 where, after the first peak, the pressure curves are much more smooth, with respect to the corresponding ones obtained by Lee et al. (2010) with the incompressible SPH scheme, and closer to the experimental results.

Moreover, it should be noted that the discrepancy with the measurements at gauges P5 and P7 occurs when the flow overpasses the top of the obstacle. During these phase, pressure values at these locations are obtained by an SPH interpolation which is based on few particles and could be strongly inaccurate. The computed pressure fluctuations could therefore as well appear as numerical artifacts due to a local and instantaneous insufficient resolution. Actually, at later times, when the contact between the top surface of the obstacle and the liquid flow is complete, the agreement with experiments is satisfactory also at these locations.

7.3 Discussion of results

From the above considerations and from the results in Fig. 5 it can be deduced that, before t=2 s, the experimental water level time-history at gauges H1 and H2 is shifted backwards due to the presence of the gate which could be responsible for a slower release of the water column than the one obtained in the SPH simulation. However, such a consideration does not apply to gauges H3 and H4 where there is much more agreement between physical and numerical results in the same time interval. After t=2.5 s the computed water profiles shows at all gauges a delay of the subsequent relative peaks. This can be slightly reduced by increasing the particles resolution that improves the prediction of the water front kinematics approaching the fixed obstacle at the bottom, but leading also to an increased computational effort.

Concerning the pressure time history at gauges P5 and P7, nonphysical oscillations before t=1.5 s have been strongly reduced at the former by increasing the number of water particles to 676500 but they are enhanced at the latter.

After the impact and partial reflection of the water wave with the downstream vertical wall, the flow is strongly conditioned by the water-air mixing process. Since the model implemented here considers only the liquid phase with no air presence, differences between the experimental and the numerical plots can arise, as previously pointed out.

It should be noted that the major discrepancies discussed above (i.e. the delay of corresponding water height peaks, the fluctuations of both water level and pressure) are common to those of Lee et al. (2010) where an analogous weakly-compressible SPH model with explicit time integration scheme has been adopted. The advantages of the proposed method for treating solid boundaries lay in the possibility to reduce the above fluctuations even with a smaller number of fluid particles, thus leading to useful results from an engineering point of view with reduced computational effort.

Moreover, it should be noted that the proposed boundary condition appears to work satisfactorily during the whole simulation: neither particle escape nor spurious reflections (with unphysical high velocities) from the boundary surfaces/edges were observed (Fig. 4).

8. CONCLUSIONS

This paper proposes a new semi-analytical technique to simulate irregular boundaries in 3D problems analyzed by the SPH method.

The portions of the boundary that give contribution to the mass and momentum equations of the generic fluid particle are considered as a material continuum (i.e. composed of an infinite number of particles) with suitable distributions of velocity and pressure. The boundary contributions can be expressed in terms of appropriate integrals extended to the volume intersection of the sphere of influence of the considered particle with the boundary surface.

Analytical details were provided with reference to the 3D flow of a slightly compressible viscous Newtonian fluid; concepts and formulas illustrated in the paper can be easily reduced to two-dimensional problems.

To prove the validity of the above procedure, a benchmark dam-break test case was simulated and the results compared with experimental data.

The analysis of the time evolution of both water level and pressure in selected points showed that the model set up can give a sound representation of the relevant physical aspects of the problem. Furthermore it reduces most of the troubles shown by a similar SPH weakly-compressible model with ghost-particle based boundary conditions, lowers the computational effort by requiring less CPU time and allows to determine the instant and magnitude of maximum water load

with the desired level of accuracy for engineering applications.
The discrepancies with respect to experimental data are partly due to the fluid particles resolution to which is related the accuracy of the prediction of the dynamic aspects (i.e. free surface evolution and pressure loads). Also the fact that the gate for initial water release and the water-air mixing effects after the impact have been neglected may represent a source of inaccuracy. The latter problem is at present under investigation. An improved version of the SPH model for the simulation of multi-phase flows is under development (Manenti et al., 2009).

ACKNOWLEDGMENTS

The Authors would like to thank the Research Fund for the Italian Electrical System that financed the project under the contract agreement between ERSE s.p.a. and the Ministry for Economic Development – General Directorate for Energy and Mining Resources stipulated on June 21st, 2007 in compliance with the Decree 73 of June 18th, 2007.
The authors wish to dedicate this paper to the memory of Dr. Andrea Maffio, colleague and friend, who shared with them the conception of this research.

NOMENCLATURE

Roman letters – scalar

c_s	Sound speed
d_i	Relative distance with respect to the i^{th} particle
h	Smoothing length
m	Generic boundary face
m_i	Mass of the i^{th} fluid particle
M	Total number of boundary faces in proximity of the i^{th} fluid particle
n_φ	Number of spherical zones
n_ϑ	Number of spherical wedges
p	Pressure of the fluid
P_i	Generic i^{th} fluid particle
r_b	Distance from P_i to the intersection between segment $\overrightarrow{P_iP}$ and the boundary face
r_{ij}	Relative distance between the i^{th} and the j^{th} fluid particles
$\tilde{r}$	Relative distance normalized by the
$\tilde{r}_b$	Distance r_b normalized by the smoothing length
R	Radius of influence
R_{ci}	Containing normal reaction for the i^{th} fluid particle
s	Space dimensions
W	Kernel function
x, y, z	Global Cartesian frame of reference

Vectors and 2nd order tensors

$\mathbf{g}$	Gravity acceleration vector
$\mathbf{l},\mathbf{m},\mathbf{n}$	Unit vectors of the local axes with respect to the global frame of reference
$\mathbf{R}$	Unit vector of the relative position between two fluid particles
$\mathbf{T}$	Transformation tensor from global to local coordinate system
$\mathbf{v}_b^{(m)}$	Velocity vector of the m^{th} boundary face (uniform)
$\mathbf{v}_i$	Velocity vector of the i^{th} fluid particle
$\mathbf{x}_i$	Position vector of the i^{th} fluid particle

Greek letters

$\overline{\alpha}_m$	Solid angle relevant to the m^{th} boundary face
α_M	Monaghan artificial viscosity parameter
$d\overline{\alpha}$	Elementary solid angle
δ	Inter-particle distance
Δt	Integration time step
ε	Compressibility modulus of fluid
μ	Dynamic viscosity of fluid
ν	Cinematic viscosity of fluid
ν'	Artificial plus cinematic viscosity of fluid
ρ	Density of the fluid particle
r, ϑ, φ	Spherical frame of reference centered on the i^{th} fluid particle
ϑ_p	Pressure smoothing non-dimensional parameter
ϑ_v	Velocity smoothing non-dimensional parameter
ξ, η, ζ	Local Cartesian frame of reference
Ω'_i	Sphere of influence of the i^{th} fluid particle inside the fluid domain
Ω''_i	Sphere of influence of the i^{th} fluid particle outside the fluid domain
Ω_i	Sphere of influence of the i^{th} fluid particle

REFERENCES

1. De Leffe M, Le Touzé D, Alessandrini B (2009). Normal flux method at the boundary

for SPH. *Proceedings of the 4th SPHERIC Workshop*. 27–29 May 2009, Nantes, France, pp. 149–156.

2. Gallati M, Braschi G (2002). Numerical description of rapidly varied flows via SPH method. *Proceedings of the IASTED International Conference on Applied Simulation and Modelling*. 25–28 June 2002, Iraklion, Greece, pp. 530–535.
3. Gingold RA, Monaghan JJ (1977). Smoothed particle hydrodynamics — Theory and application to non-spherical stars. *Monthly Notices of the Royal Astronomical Society* 181:375–389.
4. Kleefsman KMT, Fekken G, Veldman AEP, Iwanowski B, Buchner B (2005). A volume of-fluid based simulation method for wave impact problems. *Journal of Computational Physics* 206:363–393.
5. Kulasegaram S, Bonet J, Lewis RW, Profit M (2004). A variational formulation based contact algorithm for rigid boundaries in two-dimensions SPH applications. *Computational Mechanics* 33:316–325.
6. Lee ES, Violeau D, Issa R, Ploix S (2010). Application of weakly compressible and truly incompressible SPH to 3-D water collapse in waterworks. *Journal of Hydraulic Research* 48 Extra Issue:50–60.
7. Libersky LD, Petschek AG, Carney TC, Hipp JR, Allahady FA (1993). High strain Lagrangian hydrodynamics. *Journal of Computational Physics* 109:67–75.
8. Liu GR, Liu MB (2003). Smoothed particle hydrodynamics-a meshfree particle method. World Scientific Publishing Co., Singapore.
9. Lucy LB (1977). A numerical approach to the testing of the fission hypothesis. *Astronomical Journal* 82:1013–1024.
10. Manenti S, Agate G, Di Monaco A, Gallati M, Maffio A, Guandalini R, Sibilla S (2009). SPH Modeling of Rapid Sediment Scour Induced by Water Flow. *Proceedings of the 33rd IAHR International Congress*. 14–19 August 2009, Vancouver, Canada, pp. 215–222.
11. Monaghan JJ (1992a). Smoothed particle hydrodynamics. *Annual Review of Astronomy and Astrophysics* 30:543–574.
12. Monaghan JJ (1992b). Simulating Free Surface Flows with SPH. *Journal of Computational Physics* 110:399–406.
13. Monaghan JJ, Cas RC, Kos A, Hallworth MA (1999). Gravity currents descending a ramp in a stratified tank. *Journal of Fluid Mechanics* 139:39–70.
14. Monaghan JJ, Kajtar JB (2009). SPH particle boundary forces for arbitrary boundaries. *Computer Physics Communications* 180:1811–1820.
15. Monaghan JJ, Kos A (1999). Solitary waves on a Cretan beach. *Journal of Waterways Port Coastal and Ocean Engineering* 125(3):145–154.
16. Monaghan JJ, Kos A (2000). Scott Russell's wave generator. *Physics of Fluids* 12(3):622–630.
17. Monaghan JJ, Kos A, Issa N (2003). Fluid motion generated by impact. *Journal of Waterways Port Coastal and Ocean Engineering* 129(6):250–259.
18. Morris JP, Fox PJ, Zhu Y (1997). Modelling low Reynolds number incompressible flows using SPH. *Journal of Computational Physics* 136:214–266.
19. Mosqueira G, Cueto-Felgueroso L, Colominas I, Navarrina F, Casteleiro M (2002). SPH approaches for free surface flows in engineering applications. *Proceedings of the 5th World Congress on Computational Mechanics*. 7–12 July 2002, Vienna, Austria, pp. 1–10.
20. Randles PW, Libersky LD (1996). Smooth particle hydrodynamics: some recent improvements and applications, *Computer Methods in Applied Mechanics and Engineering* 139:375–408.
21. Vila JP (1999). On particle weighted methods and smooth particle hydrodynamics. *Mathematical Models and Methods in Applied Sciences* 9:161–209.